International Journal of Rock Mechanics & Mining Sciences 145 (2021) 104840

Contents lists available at ScienceDirect

International Journal of Rock Mechanics and Mining Sciences

journal homepage: www.elsevier.com/locate/ijrmms

A meso-mechanical approach to time-dependent deformation and fracturing of partially saturated sandstone

Teng-Fei Fu [a], Tao Xu [a,*], Philip G. Meredith [b], Thomas M. Mitchell [b], Michael J. Heap [c,d], Yoshitaka Nara [e]

[a] Center for Rock Instability and Seismicity Research, Northeastern University, Shenyang, 110819, China
[b] Rock & Ice Physics Laboratory, Department of Earth Sciences, University College London, Gower Street, London, WC1E6BT, UK
[c] Université de Strasbourg, CNRS, Institut Terre et Environnement de Strasbourg, UMR 7063, 5 rue René Descartes, Strasbourg F-67084, France
[d] Institut Universitaire de France (IUF), 1 rue Descartes, Paris 75231, France
[e] Department of Civil and Earth Resources Engineering, Graduate School of Engineering, Kyoto University, Kyoto Daigaku Katsura, Nishikyo-ku, Kyoto, 615-8540, Japan

ARTICLE INFO

Keywords:
Water weakening
Voronoi polyhedra
Capillary suction
Stress corrosion
Mesoscale

ABSTRACT

In the present paper, we investigate how water acts to weaken rock in two complementary ways: mechanically through the generalized effective stress principle, and chemically through time-dependent rock-fluid reactions that allow subcritical crack growth. These processes, together with capillary suction and stress corrosion, were incorporated into a three-dimensional discrete element grain-based model to investigate both the time-independent and the time-dependent mechanical behavior of partially saturated sandstone at the mesoscale. The capillary parameters related to capillary suction and subcritical parameters related to stress corrosion in the model were calibrated to match the deformation behavior of partially saturated sandstone observed in laboratory. Following this calibration, numerical simulations of partially saturated sandstone with different levels of saturation were performed in uniaxial compression. The simulations show that both the peak strength and elastic modulus of the sandstone decrease as a function of increasing saturation and that the relationships between these properties can be expressed by negative exponential functions. The simulations are in good agreement with the experimental results. Second, the long-term brittle deformation of partially saturated sandstone with different levels of saturation under a constant stress level was modeled. The results show that time-to-failure during brittle creep decreases, and the initial strain and the minimum creep strain rate increases, as a function of increasing saturation, as also observed in laboratory. The simulations also highlight the formation of tensile cracks as the main deformation mechanism during brittle creep. Finally, brittle creep in partially saturated sandstone samples with different levels of saturation was studied under different stress levels. These simulations show that the minimum creep strain rate and the time-to-failure as a function of stress can be well described by exponential relations. We conclude that the proposed model permits a deeper understanding of time-independent and time-dependent deformation and failure of partially saturated sandstone at the mesoscale.

1. Introduction

The majority of rocks forming the Earth's crust exhibit complex mechanical behavior associated with their internal microstructure and the presence of water.[1,2] Rock microstructure is one of the main factors controlling the progressive failure of rocks, which involves the sequential closure, nucleation, interaction and coalescence of microcracks, eventually resulting in macroscopic failure.[1,3–5] Water and other aqueous solutions are ubiquitous in the Earth's brittle upper crust, and the majority of the void space in rocks usually contains a fluid phase. The effect of water on the strength and other physical properties of rock is important for understanding the deformation, damage and failure processes of rocks in nature. The presence of water within rock mass is also essential to influence long-term stability of the rock mass surrounding structures, such as repositories of radioactive wastes in underground, caverns to store liquid natural gas (LNG) or liquid petroleum gas (LPG), rock slopes or the pillars and mining rooms in mining engineering.[6–10]

* Corresponding author.
E-mail address: xutao@mail.neu.edu.cn (T. Xu).

https://doi.org/10.1016/j.ijrmms.2021.104840
Received 25 February 2020; Received in revised form 3 June 2021; Accepted 22 June 2021
Available online 24 July 2021

The influence of water on the strength and deformability of sedimentary rocks has been widely studied.[1,11–24] Hawkins and McConnell,[25] for example, summarized the influence of water content on the mechanical behavior of 35 different British sandstones and found a reduction in the unconfined compressive strength (UCS) between dry and saturated conditions that varied from 8.2% for siliceous sandstones up to 78.1% for the case of clay-rich sandstones. Vásárhelyi[26] re-analyzed the UCS and Young's modulus (E) data of Hawkins and McConnell established a linear regression relation between the petrophysical constants of the dry and saturated materials. Erguler[27] presented a quantitative analysis of the effects of water content on the mechanical properties of rock, and developed a method for estimating the strength and deformability properties at any water content based on their physical properties. Verstrynge et al.[28] applied a multi-scale experimental investigation, including mineralogical analysis, non-destructive testing (X-ray microfocus computed tomography and acoustic emission) and mechanical testing, to observe the influence of moisture on the mechanical behavior of ferruginous sandstone from the micro to the macro scale. Masuda[16] performed a series of systematic creep experiments on granite and andesite both in the dry and wet states and showed that water leads to a greater strain rate sensitivity of the failure stress. However, these analyses were qualitative descriptions based on laboratory observations rather than quantitative expressions. Heap et al.[13] reviewed the available data on water-weakening in sandstone and found that the strength reduction in the presence of water increases as a function of increasing clay content.

The main underlying physical mechanisms that promote the observed reduction in rock strength in the presence of water include fracture energy reduction, capillary tension decrease, pore pressure increase, friction reduction, and chemical and corrosive deterioration.[29–31] None of these mechanisms can be discounted outright, but some are more important than others for certain rock types and loading conditions. The presence of water within rock influences rock deformation in two ways.[1,29,32–34] Mechanically, stress is partitioned between the rock matrix and the pore fluid. Pressurized pore fluids act to reduce all the applied normal stresses and thus tend to weaken and embrittle rocks. A marked decrease in strength is also observed with an increase in moisture content in rocks, which can be explained by the capillary effect.[29,35–37] Chemically, rock-fluid interaction occurs through stress corrosion reactions between water molecules and strained atomic bonds at the tips of microcracks.[22,30,38–41] Many investigators have shown evidence that capillary tensions contribute to enhancement of the strength of rock. Schmitt et al.[42] explained that water-weakening in Tournemire shale and Vosges sandstone could be attributed to the release of capillary suction between grains, which was linked to pore size distribution. West[35] and Rozhko[36] investigated capillary phenomena in partially-saturated sandstone and adopted the effective stress principle as an interpretation of the effect of moisture on the strength of rocks.

Stress corrosion is the main mechanism of time-dependent, subcritical crack growth in shallow crustal conditions (upper 20 km).[8,30,38,43] Stress corrosion is driven by reactions that occur between a chemically activated geological fluid (commonly water) and the strained crack tip bonds, such as the hydrolysis of silicon-oxygen bonds in a quartz-water system.[32,38,43–48] The strained crack tip bonds result in a weakened (activated) state that can be broken at lower stresses than unaffected bonds. Waza et al.[49] investigated experimentally the effect of water on the velocity of crack propagation in an andesite and a basalt, and showed the velocity of crack growth in water-saturated rocks was 2–3 orders of magnitude greater than in room-dry samples. Nara et al.[50–52] concluded that, when the relative humidity of the air was higher, the subcritical crack growth index tended to be lower, and the subcritical crack growth index at 90% relative humidity became close to the value in liquid water. Kranz et al.[53] found that the time-to-failure for Westerly granite during brittle creep experiments was significantly reduced in the presence of water. Tang et al.[18] studied the influence of water saturation on the long-term strength of sandstone. For samples pre-immersed in water, these authors found that the minimum creep rate and the time-to-failure increased and decreased, respectively, as a function of the duration of pre-immersion.

The main object of the present paper is to further advance our understanding of the mechanical behavior of partially saturated sandstone with different levels of water saturation at the mesoscale. For this purpose, we considered that water retained in rock acts to reduce rock strength in two ways: mechanically through the generalized effective stress principle and chemically through stress corrosion reactions. A three-dimensional discrete element grain-based model (3DEC-GBM) that accounts for both the mechanical and chemical effects was built to explore the short- and long-term mechanical behavior of sandstone with different levels of saturation on the mesoscale. A calibration procedure to determine the grain scale parameters for the model was first conducted according to the macroscopic response of sandstone deformed in laboratory experiments (e.g., uniaxial compression strength tests and uniaxial compressive creep tests). Following this validation, we then performed a series of uniaxial compressive strength simulations and uniaxial compressive creep simulations with different levels of water saturation to analyze the influence of water saturation on the mechanical properties of the studied Yunnan sandstone.

2. Numerical model

2.1. Three-dimensional discrete element grain-based model

The constituent minerals of Yunnan sandstone, collected in Yunnan (China), are quartz (60%), feldspar (19%), calcite (8%), and cement (13%) (Fig. 1a). The grain size of Yunnan sandstone is approximately 100–200 μm. The average dry density is 2061 kg/m^3, and the average porosity, calculated using mercury intrusion porosimetry, is 7.9%. A three-dimensional discrete element grain-based model (3DEC-GBM), consisting of an assemblage of Voronoi polyhedra grains with variable sizes and shapes, was built to capture the key meso-structural features and arrangement of mineral grains within the rock in a realistic manner (Fig. 1b).[54–57] The model provides a good representation of the microstructure of the studied sandstone (compare Fig. 1a and b). In this study, we generated numerical cylindrical specimens with a diameter of 50 mm and a length of 100 mm (the same dimensions as for the laboratory experiments described later in this paper) in order to deform them numerically. The specimen with 5300 Voronoi polyhedral grains that is consistent with the discretization of the numerical specimens used in previous studies[54,57] is constructed. Equivalent diameters (i.e. diameter of the sphere of equivalent volume) of the grains in the model follow a log-normal distribution, in which the logarithmic mean and logarithmic standard deviation are 1 and 0.35, respectively. The sphericity (i.e. the ratio of the surface area of the sphere of equivalent volume to the surface area of the grain) of the grains in the model also follows a log-normal distribution, in which the logarithmic mean and logarithmic standard deviation are 0.145 and 0.03, respectively.

Within the 3DEC-GBM, the macroscopic behavior of specimens is controlled by both the grains and the grain contacts. In the model, the grains are considered to be deformable and are assigned to be linear elastic without an ultimate strength. Further, the contacts between grains are automatically divided into several triangular sub-contacts after the entire grain is zoned. These sub-contacts between the deformable grains follow two contact criteria: Rankine's maximum tensile stress criterion and the Mohr-Coulomb shear failure criterion,[54] as shown in Fig. 2.

The crucial step in 3DEC-GBM is to select appropriate meso-properties of both the grains and the grain contacts according to the known macro-properties of the rock. Using a "trial-and-error" method,[58,59] numerical modeling was performed on cylindrical specimens (100 mm in length and 50 mm in diameter), and the input parameters were varied until the mechanical behavior, strength, and

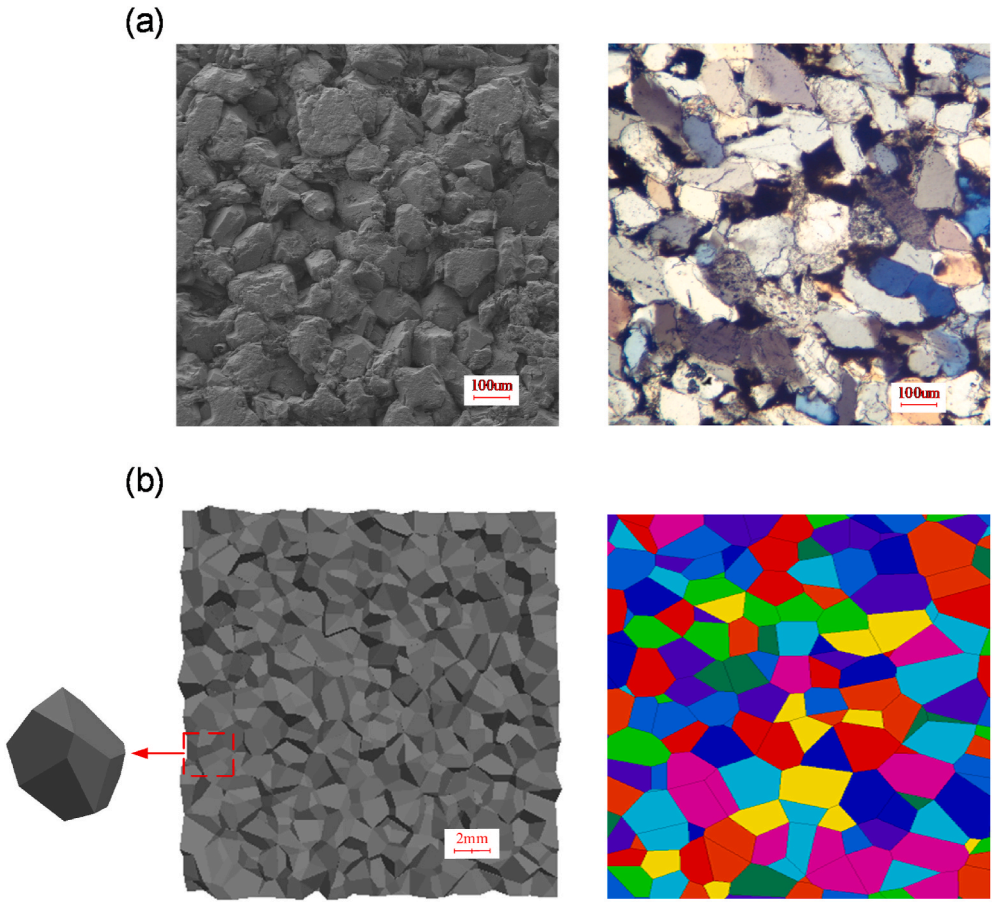

Fig. 1. (a) Scanning electron microscope (SEM) image (left) and optical microscope image (right) of Yunnan sandstone. (b) Three dimensional Voronoi tessellation (left) designed to replicate the grain scale properties of the sandstone and a section of the cubic sample (right).

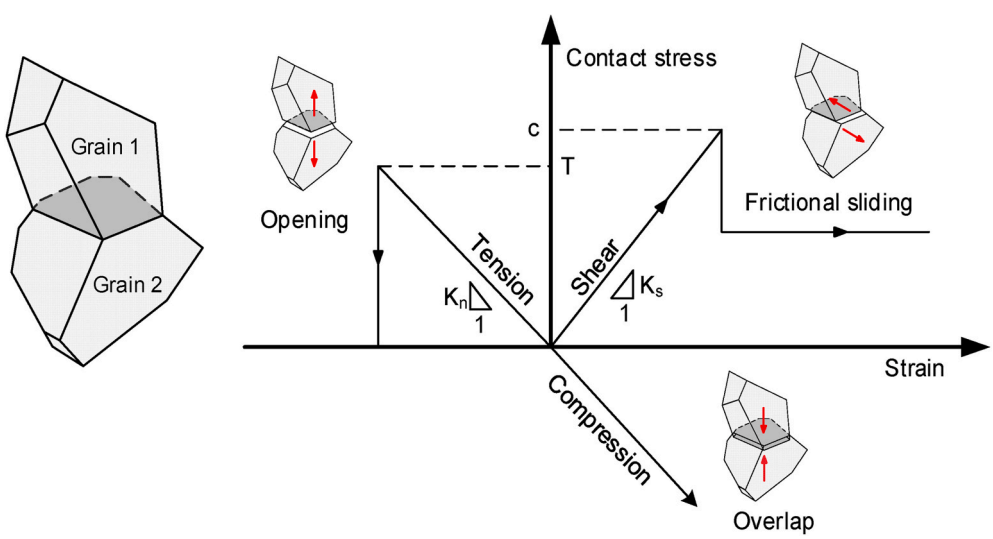

Fig. 2. Stress-strain graph showing the constitutive behavior of sub-contact between the deformable grains. Sub-contacts can fail (open), slide, or overlap. Kn – normal stiffness of the sub-contact; Ks – shear stiffness of the sub-contact. Redrawn from Ghazvinian et al.[54].

failure patterns of the numerical simulation closely matched the data and observations from laboratory experiments of the studied sandstone. We highlight that only one type of grain and one type of contact were considered in the parametric calibration performed in this paper, which means that the effects of mineral heterogeneity were explicitly not considered.

2.2. Capillary pressure related generalized effective stress

Many crustal rocks (e.g., the studied Yunnan sandstone; Fig. 1) are composed of interlocking mineral grains and microstructural defects (e.g. pores, microcracks and grain boundaries). Amongst these microstructural defects, the primary channels for fluid transport are provided

by the larger pores (often simply called "pores" or "nodal pores") connected via narrow pore-like channels (usually known as "pore throats"), while the storage volume for fluids such as water is provided by the total available void space.[60–63] Under partially saturation conditions, only a proportion of the available void space is saturated with fluid. According to the capillary law,[64] water bridges are more likely to initially invade and saturate the pores with smaller apertures (see Fig. 3). The capillary effect occurs whenever the pore space is partially-saturated with at least two immiscible fluids, such as gas and water.[64–66] Capillary pressure is created by liquid menisci in the pores between mineral grains. It has been demonstrated that water-weakening in partially-saturated rocks can be attributed to a decrease in capillary tension.[29,35,36,42,67–70]

To explain the influence of water on mechanical behavior of rock under partially saturated conditions, Rozhko[36] and Schmitt et al.[42] introduced a generalized effective stress law, established for rocks partially-saturated with air and water:

$$\sigma' = \sigma - u_a + \lambda(u_a - u_w) \tag{1}$$

where σ' is the effective stress, σ is the total stress, and λ is the additive coefficient which is equal to the degree of saturation S_e. We further assume that the total air pressure is equal to the prevailing atmospheric pressure, $u_a = 101.325$ kPa.

The formulation used to describe the relationship between capillary pressure and saturation is implemented as follows:[71]

$$P_c(s_e, \mathrm{b}) = u_a - u_w = \alpha\rho_w g \frac{b_0}{b}\left(s_e^{\frac{\beta}{1-\beta}} - 1\right)^{1/\beta} \tag{2}$$

where S_e is the saturation degree, b_0 is the relative specific aperture corresponding to the saturation of the pore throat, b is the local pore throat aperture, g is the acceleration due to gravity, ρ_w is the density of water, and α and β are constants related to capillary pressure curves. Eq.

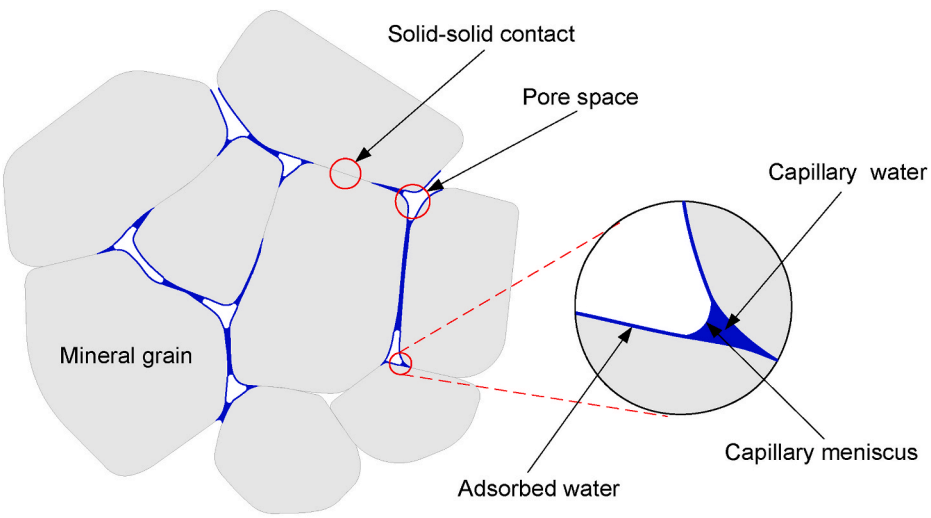

(a)

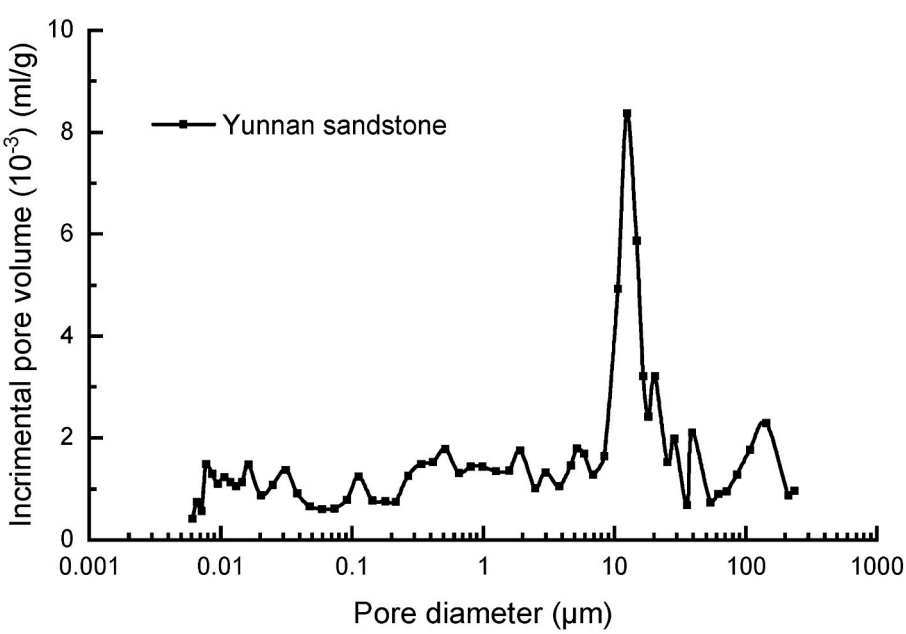

(b)

Fig. 3. (a) Schematic illustration of a representative elementary volume of partially saturated sandstone. The mineral grains were bonded and the moisture transport through grain boundary or pore. The parts with a smaller pore aperture are saturated initially according to the capillarity law. (b) The relationship of incremental pore volume and pore diameters of the studied sandstone in mercury intrusion porosimetry tests. (c) Smooth parallel-plate model on grain contacts where sub-contacts correspond to parallel-plate subregions containing solid-solid contact points and pore space whose aperture is a constant value.

Fig. 3. (*continued*).

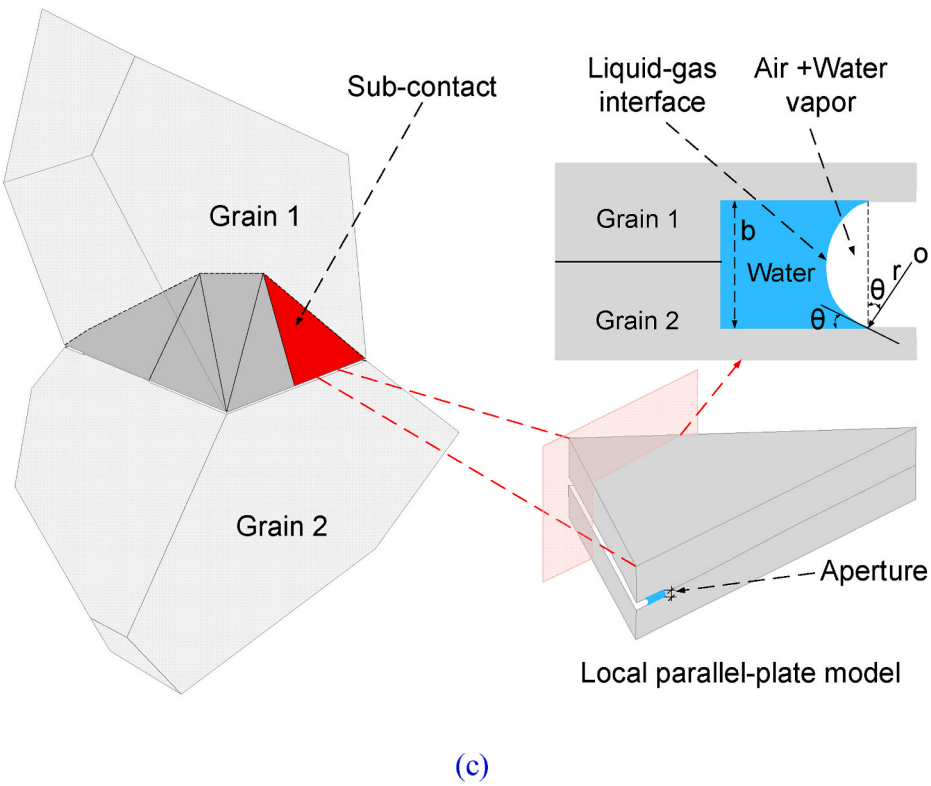

(2) has the same form as the van Genuchten curve[72], but takes into account the effect of pore throat aperture.

The formulation of a generalized effective stress can then be obtained from Eqs. (1) and (2):

$$\sigma' = \sigma + \alpha\rho_w g \frac{S_e b_0}{b}\left(s_e^{\frac{\beta}{1-\beta}} - 1\right)^{1/\beta} - u_a \tag{3}$$

This generalized effective stress law is introduced into the three-dimensional discrete element grain-based model (3DEC-GBM) to mimic the time-independent mechanical behavior of the partially saturated Yunnan sandstone. The microstructural defect network within the rock comprises rough-walled pathways in nature and water is therefore not uniformly distributed in the network of pores, pore throats and microcracks in the rock (Fig. 3a).[73] The relationship of incremental pore volume and pore diameters of the studied sandstone follow an approximately lognormal function (Fig. 3b). The median pore diameter of the pores is of the order of 100 nm. In our model, the mean grain size of grains within the specimen was set to be significantly larger than the actual mineral grains of the studied sandstone. We assume that the apertures of the sub-contacts scale by the same factor, and that these apertures fall in the range of 1–60 μm. We implemented the local parallel-plate model into the sub-contacts to represent the unevenly distributed pockets of fluid in the partially saturated sandstone. The contact between grains is automatically divided into several triangular sub-contacts after the entire grain is zoned, and each sub-contact comprises the partial boundary of the contact (Fig. 3c). Each sub-contact can be treated as a representative element volume that comprises solid-solid contact points and pore space located along the grain triple junction.

Because the grain size of our model is much larger than the aperture of the sub-contact between grains, it is likely that locally the air-water interface at the pore space is elongated in shape, parallel to the contact plane (Fig. 3c). The contact-parallel curvature is smaller than the contact-perpendicular curvature, and the magnitude of the principal curvature radii is about 10 μm. Therefore, we are conservative and assume that the capillary pressure is given in parallel plate geometry, which is the lower of the two extremes presented (parallel plates and circular). The pore spaces are simplified as two parallel plates with a constant aperture value (Fig. 3c). The interface between liquid and air is curved and often called the meniscus. The front of the meniscus is connected to the atmosphere containing air and water vapor (Fig. 3c). The pressure on both sides of the meniscus is discontinuous. The pressure in the water at the rear of the meniscus is usually lower than the atmospheric pressure. This pressure difference called capillary pressure (P_c) is expressed by the Young-Laplace equation:$P_c = 2\gamma\cos\theta/\mathrm{b}$, where γ is the interfacial tension, θ is the contact angle between the water interface and the solid (pore throat) surface, measured through the wetting phase, r is the radius of curvature, and b is the aperture of the two parallel plates. Once the normal stress or shear stress at the sub-contact exceeds the tensile strength or shear strength at the sub-contact, respectively, the sub-contacts fail and form microcracks at the solid-solid contact points.

For a contact between grains, according to the capillary law, the water occupies and saturates the sub-contacts with smaller apertures, and all sub-contacts with larger apertures contain air and water vapor. The saturation degree of the contact is given by:

$$S_e = \frac{\sum_i^m b_i A_i}{\sum_i^n b_i A_i} \tag{4}$$

where b_i is aperture of the ith sub-contact of the contact, A_i is area of the sub-contact of the contact, n is the total number of sub-contacts of the contact, m is the number of sub-contacts with smaller apertures than aperture (b_c). Each saturation degree in the model corresponds to an aperture (b_c), and the sub-contacts with an aperture less than b_c are occupied by water. In our model, the aperture of the sub-contacts range is assumed as 1–60 μm.

Our implementation of the generalized effective stress law is based on the following assumptions: (1) both tensile and shear failure criteria of the rock are expressed in terms of the generalized effective stress, not

the total stress; (2) when the saturation level within samples is constant, the saturation level of the sub-contacts in the samples, which is determined from the sub-contact aperture, is also constant; and (3) the capillary phenomenon only occurs at sub-contacts between grains and does not affect the grains themselves. The capillary pressure affects the normal deformation of the sub-contact.

2.3. Saturation related stress corrosion theory

Stress corrosion, a weakening reaction of the bond structure in rock through chemical reaction with the pore fluid, is considered to be one of the key factors driving the time-dependent deformation behavior of rocks in the upper crust (e.g., Atkinson[30]). It is well known that the presence of water greatly affects the rate of stress corrosion cracking in rock.[8,30,38,43,49,50,74,75] The most common formulation to describe a stress-induced stress corrosion process under the influence of a corrosive environment (commonly water or some aqueous solution) and reaction site stress is given by Eq. (5) based on chemical reaction rate theory.[29,31,38,44,76] The subcritical crack growth velocity is proportional to the rate of chemical reaction.[76]

$$v = v_o \exp\left(-\frac{E^*(0) - V^*\sigma + c\sigma^2 + \Gamma V_m/2\rho}{RT}\right) \tag{5}$$

where V^* is the activation volume for the surface corrosion process, $E^*(0)$ is the activation energy for surface corrosion at a stress-free surface, $c\sigma^2$ is the combined effect of a second order term in the expansion of the activation energy and the loss of strain energy due to corrosion, R is the universal gas constant, T is the absolute temperature, and $\Gamma V_m/2\rho$ represents the influence of curvature of the reaction surface. In the expression$\Gamma V_m/2\rho$, ρ is the radius of curvature of the crack tip, V_m is the molar volume of the rock, and Γ is the surface free energy of the rock corrosion interface. Because σ^2 and Γ are small in comparison to the other terms in Eq. (5), they can be neglected to a good approximation.[76] Eq. (5) can then be simplified to:

$$v = v_o \exp\left(-\frac{E^*(0) - V^*\sigma}{RT}\right) \tag{6}$$

The term $E^*(0)$ in Eq. (6) is related to the environment and is expressed as the difference in chemical potential between the reactants and products of the corrosion reaction, as follows:

$$E^*(\mathrm{O}) = \mu_{B^*} - \mu_B - n\mu_{H_2O} \tag{7}$$

where n is a material constant known as the stress corrosion index, and μ_{B^*}, μ_B, and μ_{H2O} are the chemical potential of the activated state, a bond, and of water, respectively. The chemical potentials of the activated and non-activated bonds are those corresponding to a stress-free, flat interface (the stress and curvature contributions are accounted for separately in Eq. (5)). Under atmospheric conditions, the stress corrosion index is assumed to be equal to unity in which the relative humidity is greater than 1%.

The chemical potentials of the reactants are given by:[43,76]

$$\mu_{H_2O} = \mu_{0s} + RT \ln a_s \tag{8}$$

where μ_{H2O} is the chemical potential of water in the saturated solution compared to its standard state (μ_{0s}), and a_s is the activity of the water, which is the amount of unbound water at the meniscus. a_s is defined as the ratio of the escaping tendency of water (f_i) to the escaping tendency of pure water with no radius of curvature (f_0) at the temperature of the experiment, which can be replaced by the ratio of the vapor pressure of water (P_i) to the vapor pressure of pure water (P_0) with no radius of curvature at the temperature of the experiment. P_i/P_0 is also defined as the humidity value at the reaction site.[39] The relative humidity at the meniscus increases with the increase of water vapor pressure. So, the chemical reaction rate is related to the water vapor rather than the concentration of liquid water at the meniscus. At a constant temperature, it is assumed that μ_{B^*}, μ_B, and μ_{0s} are independent of environment. It is worth noting that the dependence of stress corrosion on the amount of water in the environment is all contained in the activity.

As a result of thermodynamic equilibrium between capillary pressure and water vapor, the water transport equilibrium is governed by the Kelvin equation (Eq. (9)).

$$\ln\frac{P_i}{P_0} = -\frac{M_w\gamma\cos\theta}{RT\rho_w b} \tag{9}$$

where M_w is the molar mass of water, and ρ_w is the density of water。

Substituting Eqs. (7)–(9) into Eq. (6), the formulation that describes the relation between the chemical reaction rate (also called subcritical crack growth velocity), saturation and reaction site stress can be obtained as follows:

$$v = \beta_1 \exp^{(\beta_2\sigma - \beta_3/b)} \tag{10}$$

where $\beta_1 = Av_o\exp((-\mu_{B^*} + \mu_B + \mu_{0s})/RT)\beta_2 = V^*/RT\beta_3 = (M_w\gamma\cos\theta)/(RT\rho_w)$, and A is the constant of proportionality between the chemical reaction rate and the degradation rate.

This stress corrosion theory and the generalized effective stress law were introduced into the three-dimensional discrete element grain-based model (3DEC-GBM) in order to mimic the long-term weakening processes in partially saturated Yunnan sandstone with different levels of saturation. We assume that stress corrosion reactions only occur at sub-contacts between deformable grains and do not affect the grains themselves. Therefore, each sub-contact is a potential reaction site. The mesoscopic mechanical properties of the sub-contacts, which are characterized by values of tensile strength and cohesion in this study, are weakened at a uniform rate that is proportional to the chemical reaction rate (Fig. 4). Once the normal stress or shear stress at the sub-contact exceeded the tensile strength or shear strength at the sub-contact, respectively, the sub-contacts failed and microcracks formed. Hence, the formulation that describes the chemical reaction rate (v) of mesoscopic mechanical properties of the sub-contacts is given by:

$$v = \begin{cases} 0 & \bar{\sigma} < \sigma_0 \\ \beta_1 e^{(\beta_2\bar{\sigma} - \beta_3/\mathrm{b_c})}, & \sigma_0 \le \bar{\sigma} < \sigma_c \\ \infty & \bar{\sigma} \ge \sigma_c \end{cases} \tag{11}$$

where σ_0 is the threshold stress (so-called activation stress) below which stress corrosion reactions cannot occur (approximately equal to 0.4 of the peak stress[77]), σ_c is the peak strength, and is the reaction-site stress which incorporates a tensile stress, a shear stress, or mixed stresses acting on the sub-contact.

When only tension force is applied to the sub-contact, the degradation rate is given by:

$$\frac{dJ_i^T}{dt} = \begin{cases} 0 & \bar{\sigma} < \sigma_0 \\ \beta_1 e^{(\beta_2\bar{\sigma} - \beta_3/\mathrm{b_c})}, & \sigma_0 \le \bar{\sigma} < \sigma_c \\ \infty & \bar{\sigma} > \sigma_c \end{cases} \tag{12}$$

where $\bar{\sigma}$is the tension stress acting on the ith sub-contact of the contact, $J_i^T$is the tension strength of the ith sub-contact of the contact, and b_c is cutoff aperture. All pores with smaller aperture ($b <= b_c$) are assumed to be saturated with the water, and the pores with larger aperture ($b > b_c$) are assumed to contain air and water vapor in the contact.

When only shear force is applied to the sub-contact, the degradation rate is given by:

$$\frac{dJ_i^c}{dt} = \begin{cases} 0 & \bar{\tau} < \sigma_0 \\ \beta_1 e^{(\beta_2\bar{\tau} - \beta_3/\mathrm{b_c})}, & \sigma_0 \le \bar{\tau} < \sigma_c \\ \infty & \bar{\tau} > \sigma_c \end{cases} \tag{13}$$

where $\bar{\tau}$ is the shear stress acting on the ith sub-contact of the contact, and J_i^c is the cohesion of the ith sub-contact of the contact.

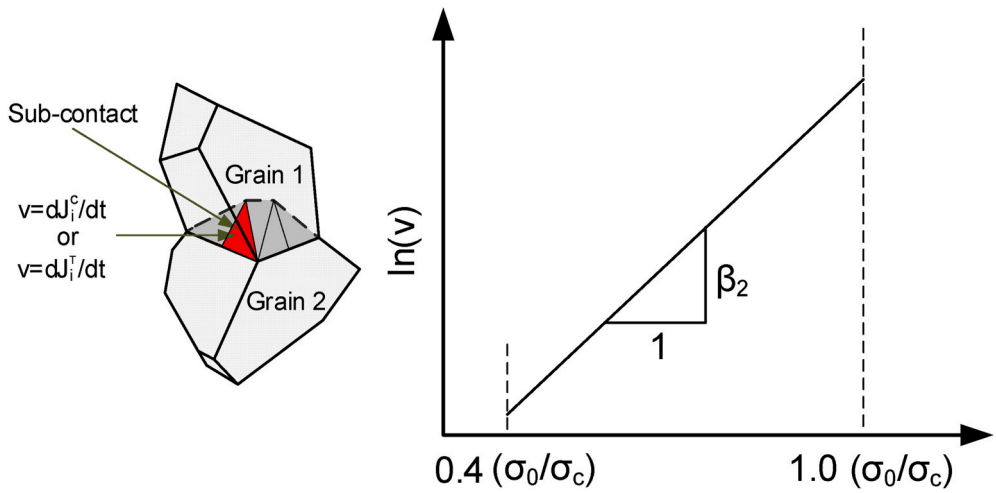

Fig. 4. Degradation rate relations for the 3DEC-GBM. σ_0 - threshold stress below which stress corrosion does not occur; σ_c - the peak strength, J_i^T and J_i^c-the tension strength and the cohesion of the *i*th sub-contact of the contact, respectively.

When mixed tensile-shear force is applied to the sub-contact, the degradation rate is obtained by utilizing the principle of superposition:

$$\frac{dJ_i^T}{dt}=\begin{cases}0 & \bar{\sigma}<\sigma_0 \text{ and } \bar{\tau}<\sigma_0\\ \beta_1 e^{(\beta_2\bar{\tau}-\beta_3/b_c)} & \sigma_0\le\bar{\sigma}\le\sigma_c \text{ and } \bar{\tau}<\sigma_0\\ \beta_1 e^{(\beta_2\bar{\tau}-\beta_3/b_c)} & \bar{\sigma}<\sigma_0 \text{ and } \sigma_0\le\bar{\tau}\le\sigma_c\\ \beta_1 e^{(\beta_2\bar{\tau}-\beta_3/b_c)}+\beta_1 e^{(\beta_2\bar{\tau}-\beta_3/b_c)} & \sigma_0\le\bar{\sigma}\le\sigma_c \text{ and } \sigma_0\le\bar{\tau}\le\sigma_c\\ \infty & \bar{\sigma}>\sigma_c or \bar{\tau}>\sigma_c\end{cases}$$

$$\frac{dJ_i^c}{dt}=\begin{cases}0 & \bar{\sigma}<\sigma_0 \text{ and } \bar{\tau}<\sigma_0\\ \beta_1 e^{(\beta_2\bar{\tau}-\beta_3/b_c)} & \sigma_0\le\bar{\sigma}\le\sigma_c \text{ and } \bar{\tau}<\sigma_0\\ \beta_1 e^{(\beta_2\bar{\tau}-\beta_3/b_c)} & \bar{\sigma}<\sigma_0 \text{ and } \sigma_0\le\bar{\tau}\le\sigma_c\\ \beta_1 e^{(\beta_2\bar{\tau}-\beta_3/b_c)}+\beta_1 e^{(\beta_2\bar{\tau}-\beta_3/b_c)} & \sigma_0\le\bar{\sigma}\le\sigma_c \text{ and } \sigma_0\le\bar{\tau}\le\sigma_c\\ \infty & \bar{\sigma}>\sigma_c or \bar{\tau}>\sigma_c\end{cases} \tag{14}$$

where $\bar{\sigma}$ and $\bar{\tau}$ are the tension and shear stress acting on the *i*th sub-contact of the contact, respectively.

When mixed compressive-shear loading is applied to the sub-contact, frictional forces are generated along the sub-contact. The shear stress $\bar{\tau}$ at the sub-contact can be substituted by the effective shear stress above friction, $\bar{\tau}-\sigma_n \tan\phi$, and the degradation rate is then given by:

$$\frac{dJ_i^c}{dt}=\begin{cases}0 & \bar{\tau}-\sigma_n\tan\phi<\sigma_0\\ \beta_1 e^{(\beta_2(\bar{\tau}-\sigma_n\tan\phi)-\beta_3/b_c)}, & \sigma_0\le\bar{\tau}-\sigma_n\tan\phi<\sigma_c\\ \infty & \bar{\tau}-\sigma_n\tan\phi>\sigma_c\end{cases} \tag{15}$$

where $\bar{\tau}$ and σ_n are the shear stress and normal stress at the sub-contact, respectively.

For time-dependent deformation in our model, the stress-corrosion time step, Δt, is taken as real time, and can be automatically adjusted via a self-adaptive procedure. The initial stress-corrosion time step is equal to 1s. When the maximum unbalanced force exceeds some threshold, the stress corrosion timestep, Δt, can be decreased by a ratio of 0.9. The specified minimum time step is 1×10^{-2} s. When the maximum unbalanced force is reduced below some threshold, the stress corrosion timestep, Δt, can be increased by a ratio of 1.1. The specified maximum time step is 1×10^{4} s. The threshold mentioned above is defined as the ratio of the maximum unbalanced force to the average gridpoint force.[78]

3. Influence of saturation on mechanical behavior of sandstone

In the present paper, the influence of water saturation on the time-independent and time-dependent mechanical behavior of Yunnan sandstone at the mesoscale was studied numerically. In order to validate our modeling approach, these numerical simulations were combined with laboratory testing. Cylindrical samples measuring 50 mm in diameter by 100 mm in length were used for both the numerical modeling and the laboratory testing. The cylindrical sandstone samples used in the laboratory tests were all drilled from a single block of Yunnan sandstone, and all in the same orientation, providing a high level of repeatability under controlled laboratory test conditions. In order to prepare sandstone samples with precise but different levels of saturation, the prepared samples were stored under controlled, constant humidity conditions, guided by vapor-liquid equilibrium theory. In this study, the saturation levels of the prepared samples were maintained constant at 13.1%, 24.3%, 45.2% and 100%, respectively.

3.1. Time-independent mechanical properties under different levels of water saturation

The stress-strain curves from uniaxial compression experiments on Yunnan sandstone under different levels of water saturation are shown in Fig. 5. These stress-strain curves are typical of those for sandstone

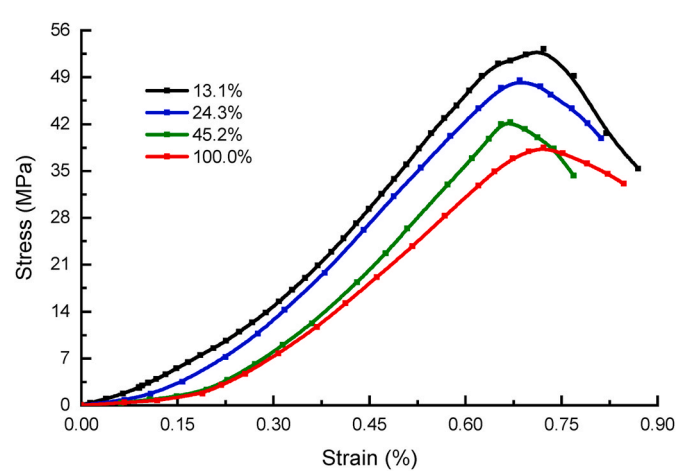

Fig. 5. Experimental uniaxial stress-strain curves for sandstone samples with different levels of saturation (from 13.1% to 100%).

deformed under uniaxial compression. Strain is first a concave-upwards, nonlinearly increasing function of stress that is commonly attributed to the closure of pre-existing defects. The stress-strain curve then becomes quasi-linear, attributed to primarily elastic deformation. Finally, the slope of the stress-strain curve decreases due to new, dilatant crack growth, with the stress eventually reaching a peak, which is the uniaxial compressive strength. This is followed by a stress drop associated with the macroscopic failure of the sample. The data of Fig. 5 also show that the uniaxial compressive strength (peak stress) of the sandstone decreases as a function of increasing saturation level. As the saturation level increased from 13.1% to 100%, the uniaxial compressive strength decreased from 52.5 MPa to 38.3 MPa. The macroscopic mechanical properties of Yunnan sandstone from our experiments at different saturation levels are summarized in Table 1. The experimental results show that the relationship between the saturation level of a specimen and its uniaxial compressive strength and elastic modulus can be well described by the following exponential relations:

$$\sigma(S_e) = 37.15 + 22.86e^{-0.034S_e} \tag{16}$$

$$E(S_e) = 8.66 + 4.53e^{-0.022S_e} \tag{17}$$

where σ is the uniaxial compressive strength, E is elastic modulus, and S_e is the level of saturation. These results are consistent with previous experimental studies that have also shown that saturation with water decreases the strength and elastic modulus of sandstone (see Heap et al.[13] and references therein).

Based on the above experimental results, a series of numerical simulations using the generalized effective stress law were conducted to determine the appropriate capillary pressure curve parameters. The calibrated capillary pressure curve parameter was found to be $\beta = 1.51$. The calibrated meso-mechanical parameters for saturated sandstone were as follows: Young's (elastic) modulus and Poisson's ratio of grains were 9.5 GPa and 0.27, respectively; normal stiffness (K_n), normal to shear stiffness ratio (K_n/K_s), cohesion (J_c), tensile strength (J_T), friction angle (ϕ) and residual friction angle (ϕ_r) of the sub-contact were 40 GPa mm^{-1}, 2, 6.1 MPa, 2.16 MPa, 27° and 6°, respectively.

The results of uniaxial compression simulations on the studied sandstone under different saturation levels are shown in Fig. 6, where the axial stress is plotted as a function of axial strain, lateral strain and volumetric strain. As expected, we observe that the numerical stress-strain curves do not contain the initial non-linear phase seen in the laboratory experimental data (Fig. 6). This is because our model does not consider the influence of initial defects and mechanical settling. However, the model is able to accurately reproduce both the mechanical behavior and strength of the sandstone beyond this initial phase.[79] Fig. 6 shows that the peak strength of simulated sandstone decreased as the saturation level was increased from 13.1% to the fully saturated state (100%). The compressive strength was reduced from 52.5 to 38.3 MPa, as the saturation level was increased from 13.1% to 100%, a reduction of close to 27% (Fig. 6). The simulations also show that the stress drop associated with macroscopic failure is less steep as the saturation level is increased (Fig. 6), indicating that the sandstone had become "softer" (less brittle) as a function of increasing water content.

During the simulations of uniaxial compression, there is no obvious influence of saturation level on the shape of the volumetric strain curves

Table 1
Macro mechanical properties of Yunnan sandstone under different saturation conditions.

Humidity/%	Water content/%	Water saturation/%	Elastic modulus/GPa	Peak strength/MPa
40%	0.8	13.1	12.1	52.5
75%	1.48	24.3	11.2	47.2
98%	2.76	45.2	10.4	42.7
Saturated	6.1	100.0	9.5	38.3

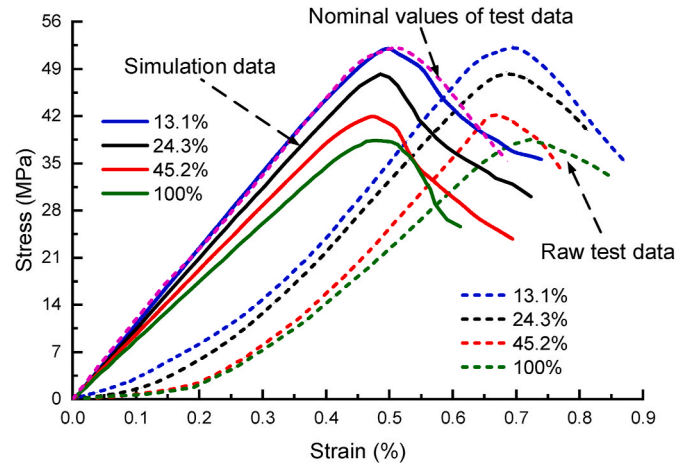

Fig. 6. Experimental and simulative stress-strain curves for a cylindrical laboratory specimen with different saturation levels (13.1, 24.3, 45.2, and 100%). The solid lines and dashed lines are the modeled and experimental stress-strain curves, respectively. In addition, the dashed pink line is the experimental stress-strain curve with a saturation level of 13.1% in which the initial non-linear part of the stress-strain curve is removed. (For interpretation of the references to colour in this figure legend, the reader is referred to the Web version of this article.)

at low stress, where the volumetric strain initially increased (volume decrease) linearly (Fig. 7). However, the volumetric strain curves began to exhibit differences for different levels of saturation at higher levels of axial stress. In particular, the switch from compaction-dominated to dilation-dominated behavior (marked by vertical dashed lines in Fig. 7) occurred at lower axial stress and lower volumetric strain as saturation level was increased. It can be inferred that the increase of humidity reduces the coefficient of friction among the cracks and that the cracks can move more easily, thus resulting in the dramatic increase in volumetric strain upon sample failure. We note that there are no systematic or significant differences in the geometry of the macroscopic shear fractures produced in the numerical samples with increasing saturation levels. Overall, however, we find that the numerical simulations accurately reproduce the mechanical behavior (e.g., the elastic modulus) and strength of the laboratory experiments (Table 2).

Fig. 7 also shows the simulated microcrack count rate as a function of axial strain. The crack count rate is still a useful tool valuable to qualitatively characterize microcrack growth and damage accumulation during the deformation process. Müller et al.[55] and Cai et al.[80] demonstrated that the numerically simulated microcrack count rates are in good agreement with the evolution of AE activity measured during laboratory experiments, and could be used to characterize the temporal evolution of microcracking and damage evolution during deformation. In the early, elastic stage of deformation, the microcrack count rate is very low, for every level of saturation (Fig. 7). The microcrack count rates then start to increase significantly once the axial stress reaches about 40% of the peak stress, again almost regardless of the level of saturation. We note that this also corresponds very closely to the transition from compaction-dominated to dilatant-dominated behavior. The microcrack count rates then increase at an even higher rate once the stress reaches about 80% of the peak stress, and reach a maximum at the peak stress for each simulation and every condition. Finally, the count rate decays steadily during the post-peak stress decrease.

Fig. 8 shows a suite of images of one of the numerical samples during deformation at a saturation level of 13.1% (images 1 to 6), and documents the progressive failure process during the simulated increase in axial stress. It can be seen that failure in the numerical sample occurs along a macroscopic shear fracture zone, with a number of minor ancillary, smaller fractures (Fig. 8, image 6). The macroscopic failure mode of the numerical samples is in good agreement with that observed

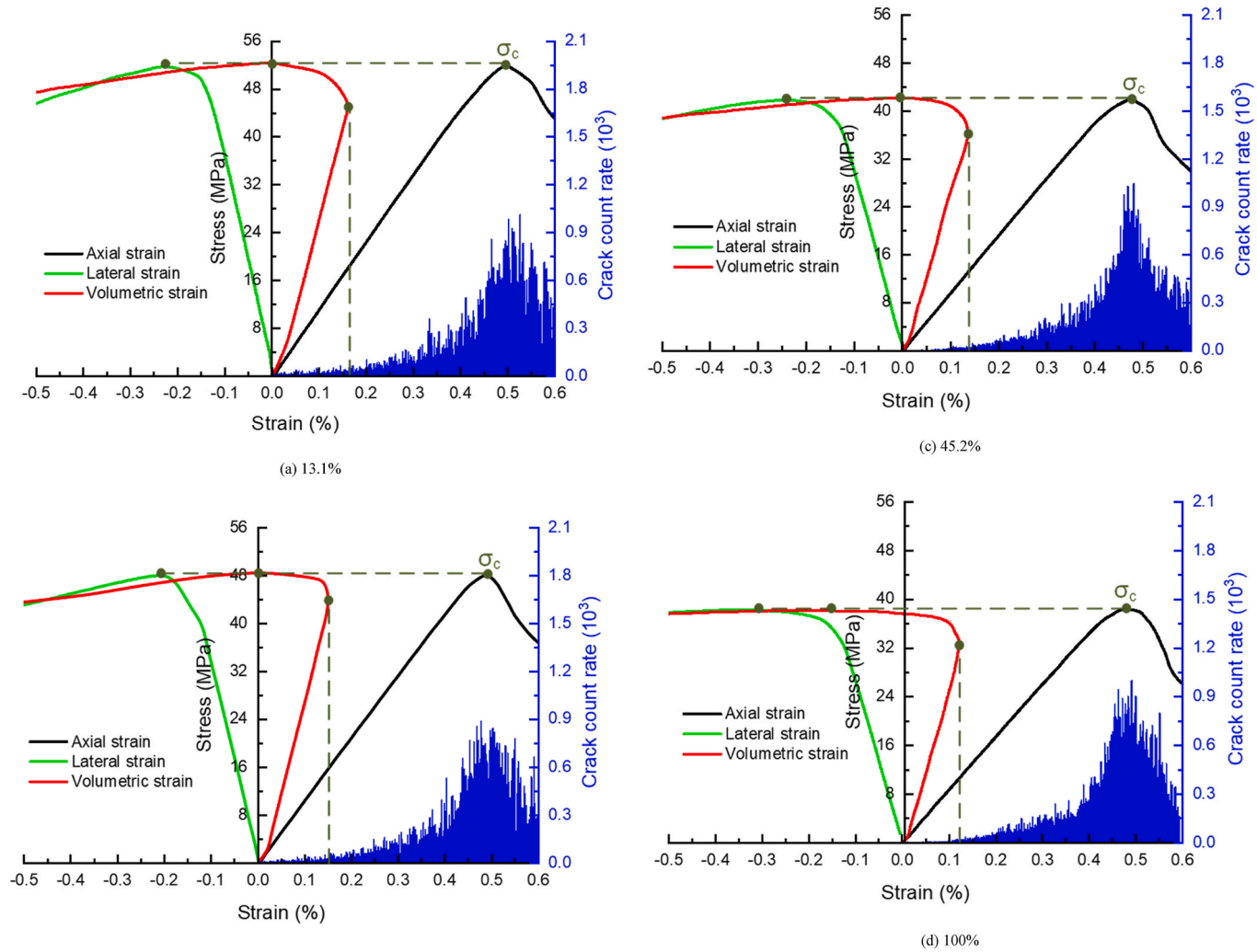

Fig. 7. Modeled stress-strain curves (axial, lateral, and volumetric strain) for cylindrical numerical specimens (100 mm in length and 50 mm in diameter) with different saturation levels (13.1%, 24.3%, 45.2% and 100%) alongside the microcrack count rates (blue histogram). (For interpretation of the references to colour in this figure legend, the reader is referred to the Web version of this article.)

Table 2
Experimental and numerical results for the uniaxial compressive strength of the studied sandstone under different saturation conditions.

Saturation	Laboratory strength/MPa	Simulated strength/MPa	Error
13.1%	52.5	52.3	0.3%
24.3%	47.2	48.1	1.9%
45.2%	42.7	42.2	1.2%
100%	38.3	38.3	0%

in the laboratory experimental sample (Fig. 8, image 7).

3.2. Time-dependent mechanical properties under different levels of water saturation

In order to study the time-dependent deformation of numerical samples under different saturation conditions, a series of numerical simulations were initially conducted, using the generalized effective stress law and stress corrosion theory, to determine the appropriate subcritical crack growth parameters. The calibrated subcritical crack growth parameters were found to be $\beta_1 = 2.9 \times 10^{-4}$, $\beta_2 = 1.56 \times 10^{-7}$ and $\beta_3 = 4.66 \times 10^{-7}$. Fig. 9 shows simulated uniaxial compressive creep curves (axial strain as a function of time) for the studied sandstone with a saturation level of 13.1%, performed at constant stresses of 70, 80, 85, 90, and 95% of the uniaxial compressive strength, σ_c, corresponding to 36.4, 41.6, 44.2, 46.8, and 49.4 MPa, respectively. In these simulations, strain first decelerates and then passes through a point of inflexion before accelerating as the sample approaches macroscopic failure; the same phenomenology as observed during brittle creep experiments in the laboratory (e.g., Brantut et al.[2]). Note that the numerical sample held at a stress level of 70% of the uniaxial compressive strength did not fail even after 100 h. For the other simulations, we observe an approximately 20-fold decrease in the time-to-failure of the numerical samples, from 3.14×10^5 to 1.66×10^4 s, as the constant creep stress is increased from 80% to 95% of σ_c (i.e. from 41.6 MPa to 49.4 MPa) (Fig. 9 and Table 3). Again, the very large decreases observed in the time-to-failure produced by the small increases in applied creep stress (Table 3), replicate those previously observed in laboratory creep experiments (see Brantut et al.[2]). This strong similarity between results from our numerical simulations and those from laboratory experiments (Table 3) lends support to our numerical methodology and approach.

Fig. 10 shows simulated creep curves (strain–time curves) and number of failed sub-contacts (a proxy for microcrack damage) as a function of elapsed time for sandstone samples with different levels of saturation (i.e. 13.1%, 24.3%, 45.2% and 100%) under a constant uniaxial creep stress of 36.61 MPa. These simulated curves also show the decelerating and accelerating creep behavior typically observed during laboratory experiments. The instantaneous strain (i.e. the strain at the

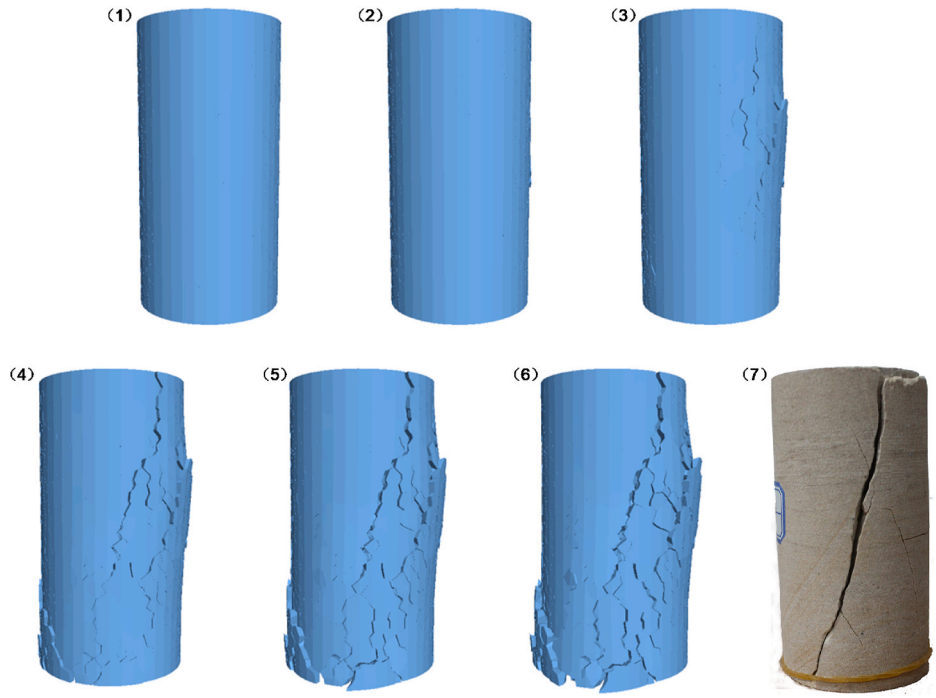

Fig. 8. Macroscopic fracture evolution in a deformed numerical specimen (images (1)–(6)) and macroscopic fracture patterns in the deformed experimental specimen (image (7)).

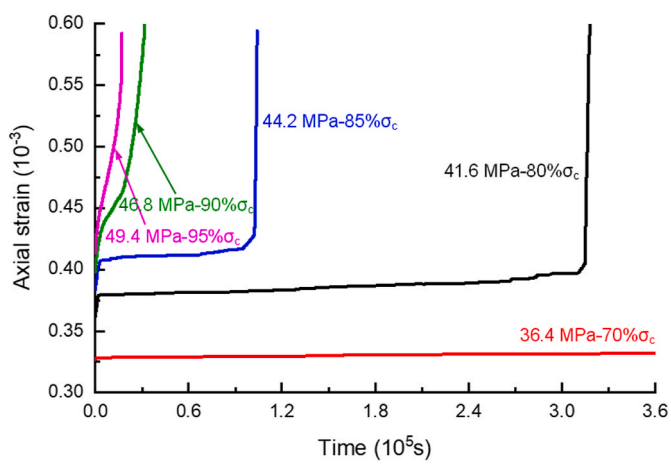

Fig. 9. Modeled uniaxial creep curves (strain–time curves) for sandstone with a saturation level of 13.1% under different constant uniaxial stresses (from 36.4 to 49.4 MPa).

Table 3
Experimental and numerical results for the time-to-failure of Yunnan sandstone with a saturation of 13.1% under different constant axial stress levels.

Peak stress/MPa	Stress level/MPa	Time to failure		error
		Laboratory/s	Simulation/s	
52.3	36.61	–	1.71×10^6	–
	41.84	3.14×10^5	3.14×10^5	0.00%
	44.46	9.72×10^4	1.05×10^5	3.39%
	47.07	4.45×10^4	3.23×10^4	27.41%
	49.69	1.60×10^4	1.66×10^4	3.75%

start of the creep portion of the simulation) increased as a function of increasing saturation level (Fig. 10). For example, as the saturation level was increased from 13.1% to 100%, the instantaneous strain increased from 0.327% to 0.391% (Fig. 10). We also observed an approximate two orders of magnitude decrease in time-to-failure (from 1.62×10^6 to 1.68×10^4 s) associated with an increase in saturation level from 13.1% to 100% (Fig. 10). The decreases in time-to-failure observed in our simulations as a function of saturation level are comparable with those reported by Kranz et al.[53] from laboratory measurements on wet and dry Westerly granite.

These results demonstrate that the rate of sub-contact breakage (microcrack damage evolution) is correlated with the decelerating and accelerating creep phases shown in Fig. 10. Overall, our simulations show that tensile microcracking dominates over shear microcracking during the creep process (Fig. 10). A relatively small number of microcracks (i.e. failed sub-contacts) was generated in the initial phase of the simulation, which weakens the internal structure of the numerical sample. The number of both tensile and shear microcracks then continued to increase slowly and the rate of microcrack formation remained almost constant for a large portion of the creep simulation. After an extended period, however, the number of microcracks (both tensile and shear) started to increase exponentially, manifested in the rapid increase in strain and the approach to instability and eventual failure of the sample (shown in Fig. 10).

The minimum creep strain rates and the times-to-failure are plotted as functions of axial stress on semi-log axes in Fig. 11a and Fig. 11b, respectively, for saturation levels of 13.1%, 24.3%, 45.2% and 100%. Fig. 11a shows that the creep strain rate for each of the four saturation levels can be well described by the following exponential relation:

$$\dot{\varepsilon} = ae^{b\sigma} \tag{18}$$

where $\dot{\varepsilon}$ is the minimum creep strain rate, σ is the uniaxial compressive creep stress, and a and b are constants. The constants a and b are different for the different saturation levels (Table 4). Fig. 11b shows that the time-to-failure for each of the four saturation levels can be well described by the following exponential relation:

$$t_f = ce^{-d\sigma} \tag{19}$$

where t_f is the time-to-failure, and c and d are constants. The constants c

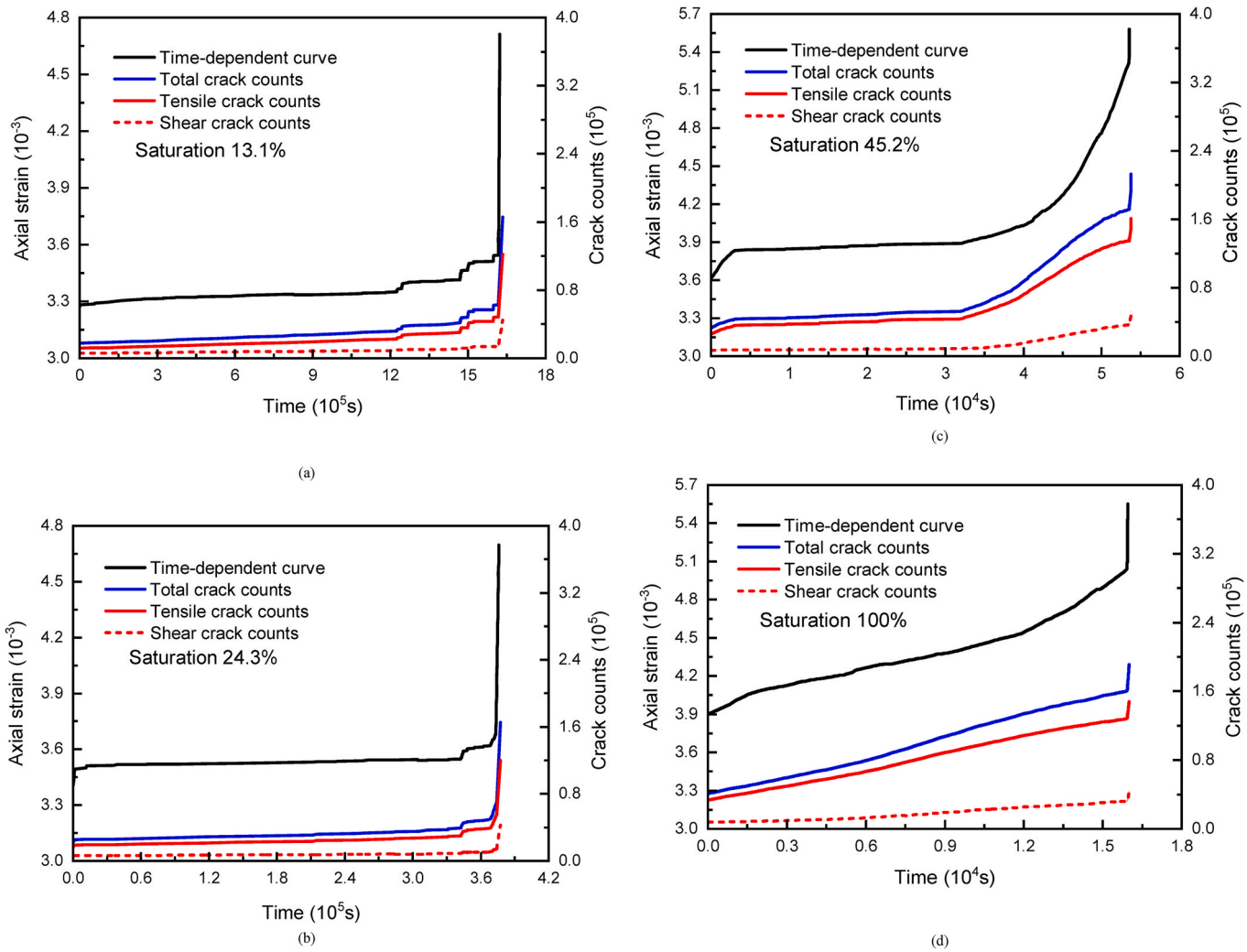

Fig. 10. Modeled uniaxial creep curves (strain–time curves) and number of crack counts as a function of time for sandstone samples with different saturation levels while maintaining a constant stress level of 36.61 MPa. (a) 13.1%, (b) 24.3%, (c) 45.2% and (d) 100%.

and *d* are also different for the different saturation levels (Table 4). Heap et al.[32,33] found that the minimum creep strain rate and the time-to-failure as functions of differential stress during triaxial brittle creep experiments on porous sandstone and microcracked basalt, respectively, could be well described by either a power law or an exponential law.

4. Discussion

The three-dimensional discrete element grain-based model (3DEC-GBM) used herein provides us with insights into the time-dependent deformation of partially saturated rock (here sandstone) with various levels of water saturation. However, although the model duplicates well the shape and arrangement of mineral grains within the rock, it is unable to reproduce in full the real grain structure and heterogeneity of the sandstone with respect to its mineral composition. This arises due to the finite limit of available computing power, so that it is impracticable to reproduce exactly the grain structure of the rock, and an element of simplification is therefore always required. Gao et al.[59,81] presented a UDEC-GBM model that incorporated a minimum grain size set at 7.6 times the actual grain of the rock in an effort to reflect grain scale heterogeneity as closely as possible. Li et al.[82] analyzed the effect of the grain size of granular brittle rocks on the macroscopic responses observed in uniaxial compression tests and Brazilian disc tests and set the grain diameter to 0.18 mm. In this study, we used cylindrical specimens (50 mm in diameter by 100 mm in length) comprising 5300 Voronoi polyhedral grains. Our numerical samples are therefore similar to the discretization of the numerical specimens used in previous studies (e.g.,54). If enhanced parallelization of 3DEC becomes available in the future, then our modeling approach can be further refined to reveal more detail of the fracture processes occurring at the mesoscale.

Ga et al.[81] and Bewick et al.[83] built a microstructural model of sandstone that contained three different minerals: feldspar (50%), quartz (20%), and calcite (30%). These authors randomly distributed the mineral grains in their model based on the actual mineral composition percentages. Chen et al.[84] and Tan et al.[85] further reproduced the actual heterogeneity with respect to mineral composition of the rock using a digital image processing (DIP) method. The DIP method provides a good basis for establishing numerical models that better account for the heterogeneous microstructure of natural rocks. In this study, only one type of grain and one type of contact are considered in the parametric study, which means that the effects of mineral heterogeneity are explicitly not considered. However, further progress in this modeling approach requires that 3DEC-GBM and DIP be combined in order to make significant advances in the study the failure mechanisms of heterogeneous rocks at the mesoscale.

Our mechanical model is also capable of simulate the influence of temperature (see Eq. (6)), but the modeling procedure used here was specifically focused on the study of the deformation behavior of rock under different levels of saturation at ambient temperature. Potential in-

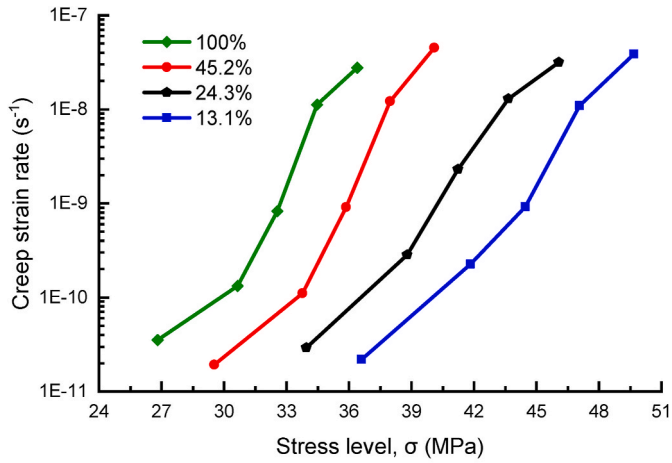

(a)

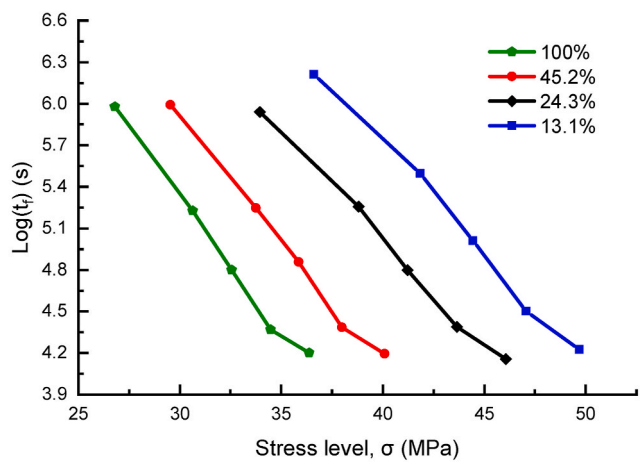

(b)

Fig. 11. Minimum creep strain rate and time-to-failure as a function of axial stress from uniaxial brittle creep simulations for sandstone samples with saturation levels of 13.1%, 24.3%, 45.2% and 100%. t_f, time-to-failure of samples.

Table 4
The constants for the creep strain rate and the time-to-failure of Yunnan sandstone under the different saturation levels.

Constants	Saturation			
	a	b	c	d
13.1%	5×10^{-19}	0.52	2.63×10^{11}	0.33
24.3%	9×10^{-17}	0.43	8.29×10^{10}	0.34
45.2%	1×10^{-19}	0.66	1.79×10^{11}	0.41
100%	3×10^{-17}	0.57	2.00×10^{11}	0.46

situ applications are therefore restricted to the shallow crust. To use our numerical model to study the long-term evolution of the Earth's crust at greater depths, it would need to be extended to incorporate more advanced constitutive models. In addition, in natural environments relevant to rock engineering or underground excavations, rock is often saturated by aqueous fluids with varying salinity and non-neutral values of pH. It is therefore essential to focus future modeling studies on the effects of, for example, salinity and pH on subcritical crack growth (i.e. stress corrosion) in rocks to have a better understanding of the time-dependent fracturing behavior of rock in real sub-surface environments. For example, Nara et al.[51,86] used the load relaxation method of the double torsion test to investigate subcritical crack growth in rock in distilled water and in an aqueous solution of sodium hydroxide (NaOH, $Ca(OH)_2$) under conditions of controlled temperature, which provide the basis for investigating the influence of electrolyte concentration on time-dependent behavior of rocks.

5. Conclusions

In the present paper, we proposed a three-dimensional discrete element grain-based model (3DEC-GBM) that incorporates the generalized effective stress principle and stress corrosion theory. We used this model to characterize the short- and long-term deformation behavior of a low-porosity sandstone with different saturation levels at the mesoscopic scale. The capillary parameters and subcritical parameters were validated against laboratory uniaxial compression experiments and brittle creep experiments under different saturation levels, respectively. We found that the model could accurately capture the mechanical behavior, strength, and failure patterns obtained in laboratory experiments (here demonstrated for Yunnan sandstone). The time-independent numerical simulations show that water can significantly degrade the mechanical property of the sandstone. The average peak strength and elastic modulus of 100% saturated specimens were reduced by 26.39% and 27.63%, respectively, compared to specimens with a saturation level of 13.1%. Further, the creep numerical simulations were performed under different saturation levels while maintaining a constant stress level. We found that the growth of macro fractures in sandstone samples is predominately due to the growth of tensile microcracks, and that the deformation in the specimen was water sensitive (i.e. the time-to-failure was reduced as the level of saturation was increased), as also reported in earlier experimental studies.[18] We also performed a set of uniaxial compressive creep simulations with different levels of saturation (i.e. 13.1%, 24.3%, 45.2%, 100%) under different constant axial stresses of 70, 80, 85, 90, and 95% of the uniaxial compressive strength. We found that creep strain rates and times-to-failure for each of the four sample types can be well described by exponential relations. The presented procedure shows new possibilities to provide a deeper understanding of the mechanical behavior of sandstone with different saturation levels in a realistic manner by explicitly considering fracture processes at the grain scale.

Declaration of competing interest

The authors declare that they have no known competing financial interests or personal relationships that could have appeared to influence the work reported in this paper.

Acknowledgments

The work was jointly supported by National Natural Science Foundation of China (51974062, 41672301, 51761135102 and 51811530312), a Royal Society International Exchange grant, United Kingdom (IEC\NSFC\170625), National Key Research and Development Program of China (2017YFC1503100), Fundamental Research Funds for the Central Universities in China (N180101028) and a Partenariats Hubert Curien (PHC) Cai Yuanpei grant, France (36605 ZB). M.J. Heap acknowledges support from the Institut Universitaire de France (IUF). The comments of Martijn van den Ende and one anonymous reviewer helped improve this manuscript.

References

1 Baud P, Zhu W, Wong TF. Failure mode and weakening effect of water on sandstone. *J Geophys Res: Solid Earth*. 2000;105(B7):16371–16389.
2 Brantut N, Heap MJ, Meredith PG, Baud P. Time-dependent cracking and brittle creep in crustal rocks: a review. *J Struct Geol*. 2013;52:17–43.
3 Sammis C, Ashby M. The failure of brittle porous solids under compressive stress states. *Acta Metall*. 1986;34(3):511–526.

4 Lockner D, Byerlee J, Kuksenko V, Ponomarev A, Sidorin A. Quasi-static fault growth and shear fracture energy in granite. *Nature*. 1991;350(6313):39–42.
5 Ashby MF, Sammis CG. The damage mechanics of brittle solids in compression. *Pure Appl Geophys*. 1990;133(3):489–521.
6 Bai H, Ma D, Chen Z. Mechanical behavior of groundwater seepage in karst collapse pillars. *Eng Geol*. 2013;164:101–106.
7 Langer M, Heusermann S. Geomechanical stability and integrity of waste disposal mines in salt structures. *Eng Geol*. 2001;61(2-3):155–161.
8 Nara Y, Morimoto K, Yoneda T, Hiroyoshi N, Kaneko K. Effects of humidity and temperature on subcritical crack growth in sandstone. *Int J Solid Struct*. 2011;48(7-8):1130–1140.
9 Iverson RM. Landslide triggering by rain infiltration. *Water Resour Res*. 2000;36(7):1897–1910.
10 Mu WQ, Li LC, Yang TH, Yu GF, Han YC. Numerical investigation on a grouting mechanism with slurry-rock coupling and shear displacement in a single rough fracture. *Bull Eng Geol Environ*. 2019;(4):1–19.
11 Dyke C, Dobereiner L. *Evaluating the Strength and Deformability of Sandstones*. vol. 24. Geological Society of London; 1991:123–134.
12 Castagna A, Ougier-Simonin A, Benson P, et al. Thermal damage and pore pressure effects of the brittle-ductile transition in comiso limestone. *J Geophys Res: Solid Earth*. 2018;123(9):7644–7660.
13 Heap MJ, Villeneuve M, Kushnir AR, Farquharson JI, Baud P, Reuschlé T. Rock mass strength and elastic modulus of the Buntsandstein: an important lithostratigraphic unit for geothermal exploitation in the Upper Rhine Graben. *Geothermics*. 2019;77:236–256.
14 Nicolas A, Fortin J, Regnet J, Dimanov A, Guéguen Y. Brittle and semi-brittle behaviours of a carbonate rock: influence of water and temperature. *Geophys J Int*. 2016;206(1):438–456.
15 Heap MJ, Brantut N, Baud P, Meredith PG. Time-dependent compaction band formation in sandstone. *J Geophys Res: Solid Earth*. 2015;120(7):4808–4830.
16 Masuda K. Effects of water on rock strength in a brittle regime. *J Struct Geol*. 2001;23(11):1653–1657.
17 Michalopoulos LP, Triandafilidi GE. Influence of water on hardness, strength and compressibility of rock. *Bull Assoc Eng Geol*. 1976;13(1):1–22.
18 Tang SB, Yu CY, Heap MJ, Chen PZ, Ren YG. The influence of water saturation on the short- and long-term mechanical behavior of red sandstone. *Rock Mech Rock Eng*. 2018;51(9):2669–2687.
19 Wong LNY, Maruvanchery V, Liu G. Water effects on rock strength and stiffness degradation. *Acta Geotechnica*. 2016;11(4):713–737.
20 Zhou Z, Cai X, Ma D, Cao W, Chen L, Zhou J. Effects of water content on fracture and mechanical behavior of sandstone with a low clay mineral content. *Eng Fract Mech*. 2018;193:47–65.
21 Zhang D, Pathegama Gamage R, Perera M, Zhang C, Wanniarachchi W. Influence of water saturation on the mechanical behaviour of low-permeability reservoir rocks. *Energies*. 2017;10(2):236.
22 Nara Y, Tanaka M, Harui T. Evaluating long-term strength of rock under changing environments from air to water. *Eng Fract Mech*. 2017;178:201–211.
23 Liu H, Zhu W, Yu Y, Xu T, Li R, Liu X. Effect of water imbibition on uniaxial compression strength of sandstone. *Int J Rock Mech Min Sci*. 2020;127:104200.
24 Xu T, Zhou G, Heap MJ, Yang S, Konietzky H, Baud P. The modeling of time-dependent deformation and fracturing of brittle rocks under varying confining and pore pressures. *Rock Mech Rock Eng*. 2018;51(10):3241–3263.
25 Hawkins A, McConnell B. Sensitivity of sandstone strength and deformability to changes in moisture content. *Q J Eng Geol Hydrogeol*. 1992;25(2):115–130.
26 Vásárhelyi B. Some observations regarding the strength and deformability of sandstones in dry and saturated conditions. *Bull Eng Geol Environ*. 2003;62(3):245–249.
27 Erguler Z, Ulusay R. Water-induced variations in mechanical properties of clay-bearing rocks. *Int J Rock Mech Min Sci*. 2009;46(2):355–370.
28 Verstrynge E, Adriaens R, Elsen J, Van Balen K. Multi-scale analysis on the influence of moisture on the mechanical behavior of ferruginous sandstone. *Construct Build Mater*. 2014;54:78–90.
29 Eeckhout EV. The mechanisms of strength reduction due to moisture in coal mine shales. *Int J Rock Mech Min Sci Geomech Abstr*. 1976;13(2):61–67.
30 Atkinson BK. Subcritical crack growth in geological materials. *J Geophys Res: Solid Earth*. 1984;89(B6):4077–4114.
31 Atkinson BK, Meredith PG. Stress corrosion cracking of quartz: a note on the influence of chemical environment. *Tectonophysics*. 1981;77(1-2):T1–T11.
32 Heap MJ, Baud P, Meredith PG, Bell AF, Main IG. Time-dependent brittle creep in Darley Dale sandstone. *J Geophys Res*. 2009;114(B7).
33 Heap MJ, Baud P, Meredith P, Vinciguerra S, Bell A, Main I. Brittle creep in basalt and its application to time-dependent volcano deformation. *Earth Planet Sci Lett*. 2011;307(1-2):71–82.
34 Scholz CH. *The Mechanics of Earthquakes and Faulting*. Cambridge University Press; 2019.
35 West G. Effect of suction on the strength of rock. *Q J Eng Geol Hydrogeol*. 1994;27(1):51–56.
36 Rozhko AY. *Capillary Phenomena in Partially-Saturated Rocks: Theory of Effective Stress. 45th US Rock Mechanics/Geomechanics Symposium*. American Rock Mechanics Association; 2011.
37 Jeong HS, Kang SS, Obara Y. Influence of surrounding environments and strain rates on the strength of rocks subjected to uniaxial compression. *Int J Rock Mech Min Sci*. 2007;44(3):321–331.
38 Atkinson BK. Subcritical crack propagation in rocks: theory, experimental results and applications. *J Struct Geol*. 1982;4(1):41–56.
39 Freiman SW. Effects of chemical environments on slow crack growth in glasses and ceramics. *J Geophys Res: Solid Earth*. 1984;89(B6):4072–4076.
40 Meredith PG, Atkinson BK. Stress corrosion and acoustic emission during tensile crack propagation in Whin Sill dolerite and other basic rocks. *Geophys J Int*. 1983;75(1):1–21.
41 Meredith PG, Atkinson BK. Fracture toughness and subcritical crack growth during high-temperature tensile deformation of Westerly granite and Black gabbro. *Phys Earth Planet In*. 1985;39(1):33–51.
42 Schmitt L, Forsans T, Santarelli F. Shale testing and capillary phenomena. *Int J Rock Mech Min Sci Geomech Abstr*. 1994;31(5):411–427.
43 Wiederhorn SM, Freiman SW, Fuller ER, Simmons C. Effects of water and other dielectrics on crack growth. *J Mater Sci*. 1982;17(12):3460–3478.
44 Charles R. Static fatigue of glass. I. *J Appl Phys*. 1958;29(11):1549–1553.
45 Charles R. Static fatigue of glass. II. *J Appl Phys*. 1958;29(11):1554–1560.
46 Xu T, Tang C-a, Zhao J, Li L, Heap M. Modelling the time-dependent rheological behaviour of heterogeneous brittle rocks. *Geophys J Int*. 2012;189(3):1781–1796.
47 Evans A. A method for evaluating the time-dependent failure characteristics of brittle materials—and its application to polycrystalline alumina. *J Mater Sci*. 1972;7(10):1137–1146.
48 Main IG, Meredith PG. Stress corrosion constitutive laws as a possible mechanism of intermediate-term and short-term seismic quiescence. *Geophys J Int*. 1991;107(2):363–372.
49 Waza T, Kurita K, Mizutani H. The effect of water on the subcritical crack growth in silicate rocks. *Tectonophysics*. 1980;67(1-2):25–34.
50 Nara Y, Hiroyoshi N, Yoneda T, Kaneko K. Effects of relative humidity and temperature on subcritical crack growth in igneous rock. *Int J Rock Mech Min Sci*. 2010;47(4):640–646.
51 Nara Y, Takada M, Igarashi T, Hiroyoshi N, Kaneko K. Subcritical crack growth in rocks in an aqueous environment. *Explor Geophys*. 2009;40(1):163–171.
52 Nara Y, Yamanaka H, Oe Y, Kaneko K. Influence of temperature and water on subcritical crack growth parameters and long-term strength for igneous rocks. *Geophys J Int*. 2013;193(1):47–60.
53 Kranz RL, Harris WJ, Carter NL. Static fatigue of granite at 200 C. *Geophys Res Lett*. 1982;9(1):1–4.
54 Ghazvinian E, Diederichs M, Quey R. 3D random Voronoi grain-based models for simulation of brittle rock damage and fabric-guided micro-fracturing. *Journal of Rock Mechanics and Geotechnical Engineering*. 2014;6(6):506–521.
55 Müller C, Frühwirt T, Haase D, Schlegel R, Konietzky H. Modeling deformation and damage of rock salt using the discrete element method. *Int J Rock Mech Min Sci*. 2018;103:230–241.
56 Wang X, Cai M. Modeling of brittle rock failure considering inter- and intra-grain contact failures. *Comput Geotech*. 2018;101:224–244.
57 Fu TF, Xu T, Heap MJ, Meredith PG, Mitchell TM. Mesoscopic time-dependent behavior of rocks based on three-dimensional discrete element grain-based model. *Comput Geotech*. 2020;121:12.
58 Farahmand K, Vazaios I, Diederichs MS, Vlachopoulos N. Investigating the scale-dependency of the geometrical and mechanical properties of a moderately jointed rock using a synthetic rock mass (SRM) approach. *Comput Geotech*. 2018;95:162–179.
59 Gao FQ, Stead D, Elmo D. Numerical simulation of microstructure of brittle rock using a grain-breakable distinct element grain-based model. *Comput Geotech*. 2016;78:203–217.
60 Bakke S, Øren PE. 3-D pore-scale modelling of sandstones and flow simulations in the pore networks. *SPE J*. 1997;2(2):136–149.
61 Wardlaw NC, Li Y, Forbes D. Pore-throat size correlation from capillary pressure curves. *Transport Porous Media*. 1987;2(6):597–614.
62 Zhang X, Sanderson DJ, Barker AJ. Numerical study of fluid flow of deforming fractured rocks using dual permeability model. *Geophys J Int*. 2002;151(2):452–468.
63 Bernabe Y. Pore geometry and pressure dependence of the transport properties in sandstones. *Int J Rock Mech Min Sci Geomech Abstr*. 1991;56(4):436.
64 Tokunaga TK, Wan J. Water film flow along fracture surfaces of porous rock. *Water Resour Res*. 1997;33(6):1287–1295.
65 Zeng Q, Wang Y, Li K. Uniform model for moisture transport in porous materials and its application to concrete at selected Chinese regions. *J Mater Civ Eng*. 2013;26(6),05014001.
66 Papamichos E, Brignoli M, Santarelli F. An experimental and theoretical study of a partially saturated collapsible rock. *Mech Cohesive-Frict Mater*. 1997;2(3):251–278.
67 Reitsma S, Kueper BH. Laboratory measurement of capillary pressure-saturation relationships in a rock fracture. *Water Resour Res*. 1994;30(4):865–878.
68 Han G, Dusseault M, Cook J. Quantifying rock capillary strength behavior in unconsolidated sandstones. In: *SPE/ISRM Rock Mechanics Conference*. Society of Petroleum Engineers; 2002.
69 Yilmaz I. Influence of water content on the strength and deformability of gypsum. *Int J Rock Mech Min Sci*. 2010;2(47):342–347.
70 Grgic D, Giot R, Homand F, Giraud A. Effect of suction on the mechanical behaviour of iron ore rock. *Int J Numer Anal Methods GeoMech*. 2005;29(8):789–827.
71 Itasca. *UDEC*. Minneapolis, MN, USA: Itasca Consulting Group Inc.; 2018.
72 Van Genuchten MT. A closed-form equation for predicting the hydraulic conductivity of unsaturated soils. *Soil Sci Soc Am J*. 1980;44(5):892–898.
73 Akhavan A, Shafaatian S-M-H, Rajabipour F. Quantifying the effects of crack width, tortuosity, and roughness on water permeability of cracked mortars. *Cement Concr Res*. 2012;42(2):313–320.
74 Nara Y, Morimoto K, Hiroyoshi N, Yoneda T, Kaneko K, Benson PM. Influence of relative humidity on fracture toughness of rock: implications for subcritical crack growth. *Int J Solid Struct*. 2012;49(18):2471–2481.

75 Wiederhorn S, Fuller ER, Thomson R. Micromechanisms of crack growth in ceramics and glasses in corrosive environments. *Met Sci*. 1980;14(8-9):450–458.
76 Wiederhorn S. Influence of water vapor on crack propagation in soda-lime glass. *J Am Ceram Soc*. 1967;50(8):407–414.
77 Potyondy DO. Simulating stress corrosion with a bonded-particle model for rock. *Int J Rock Mech Min Sci*. 2007;44(5):677–691.
78 Itasca. *3DEC. Minneapolis*. MN, USA: Itasca Consulting Group Inc; 2013.
79 Xu T, Fu TF, Heap MJ, Meredith PG, Baud P. Mesoscopic damage and fracturing of heterogeneous brittle rocks based on three-dimensional polycrystalline discrete element method. *Rock Mech Rock Eng*. 2020;(23).
80 Cai M, Kaiser P, Morioka H, et al. FLAC/PFC coupled numerical simulation of AE in large-scale underground excavations. *Int J Rock Mech Min Sci*. 2007;44(4):550–564.
81 Gao F, Kang H. Grain-based discrete-element modeling study on the effects of cementation on the mechanical behavior of low-porosity brittle rocks. *Int J GeoMech*. 2017;17(9).
82 Li XF, Li HB, Zhao Y. 3D polycrystalline discrete element method (3PDEM) for simulation of crack initiation and propagation in granular rock. *Comput Geotech*. 2017;90:96–112.
83 Bewick RP, Kaiser PK, Bawden WF, Bahrani N. DEM simulation of direct shear: 1. Rupture under constant normal stress boundary conditions. *Rock Mech Rock Eng*. 2013;47(5):1647–1671.
84 Chen W, Konietzky H, Liu C, Tan X. Hydraulic fracturing simulation for heterogeneous granite by discrete element method. *Comput Geotech*. 2018;95:1–15.
85 Tan X, Konietzky H, Chen W. Numerical simulation of heterogeneous rock using discrete element model based on digital image processing. *Rock Mech Rock Eng*. 2016;49(12):4957–4964.
86 Nara Y, Takeda H. Subcritical crack growth in sandstone in aqueous environment with different calcium ion concentration. *Procedia Structural Integrity*. 2018;13: 222–225.